ORIGINAL ARTICLE

Sensitivity of dryland vegetation patterns to storm characteristics

Octavia V. Crompton[1,2] | **Sally E. Thompson**[2,3]

[1]Department of Earth and Planetary Sciences, University of California, Berkeley, CA, USA.

[2]Department of Civil and Environmental Engineering, University of California, Berkeley, CA, USA.

[3]Department of Environmental Engineering, University of Western Australia, Perth, WA, Australia.

Correspondence
Octavia Crompton, Department of Civil and Environmental Engineering, University of California Berkeley, Berkeley, California, 94720, USA
Email: octavia@berkeley.edu

Funding information
National Science Foundation, EAR-1331940

Running Title
Sensitivity of dryland vegetation patterns to storm characteristics

Ecohydrological phenomena are often multiscale in nature, with behavior that emerges from the interaction of tightly coupled systems having characteristic timescales that differ by orders of magnitude. Models address these differences using timescale separation methods, where each system is held in psuedo-steady state while the other evolves. When the computational demands of solving the 'fast' system are large, this strategy can become numerically intractable. Here, we use emulation modeling to accelerate the simulation of a computationally intensive 'fast' system: overland flow. We focus on dryland ecosystems in which storms generate overland flow, on timescales of 10^{1-2}s. In these ecosystems overland flow delivers crucial water inputs to vegetation, which grows and disperses 'slowly', on timescales of 10^{7-9}s. Emulation allows for a physically realistic treatment of flow, advancing on phenomenological descriptions used in previous studies. Resolving the within-storm processes reveals novel dynamics, including new transition pathways from patchy vegetation to desertification, that are specifically controlled by storm processes.

KEYWORDS
model emulation, pattern formation, arid ecosystems, multiscale, overland flow

1 | INTRODUCTION

Multiscale behavior, in which tightly-coupled processes have characteristic spatial and/or temporal scales that differ by orders of magnitude, is ubiquitous in environmental systems (Blöschl and Sivapalan, 1995), including ecohydrological systems (Thompson et al., 2011b). Multiscale behavior fundamentally challenges the measurement and characterization of, and predictions about these systems. One approach to addressing multiscale behavior is to identify scales that separate processes from each other - for example, the 'spectral gap' in atmospheric turbulence allows mean wind speeds to be treated as pseudo-steady over hourly or shorter timescales, during which turbulent fluctuations dominate variability (Katul et al., 2001; Fiedler and Panofsky, 1970). Such scale separations allow the dynamics of 'slow' and 'fast' processes to be separately described and simulated at their appropriate timescale, while holding the other process in pseudo-steady state (Murray, 2003). This approach is used to solve stiff problems in systems such as enzyme kinetics (Michaelis and Menten, 1913; Briggs and Haldane, 1925; Murray, 2003). One limitation of timescale separation approaches, however, is that many iterations of the fast process are needed while resolving the dynamics of the slow process. If the fast process is computationally intensive, this can render timescale separation computationally infeasible.

Multiple scales in ecohydrological systems are susceptible to this computational challenge. For example, in dryland ecosystems, infrequent but intense storm events generate runoff on bare soil sites, which then infiltrates beneath vegetation canopies (Schlesinger and Pilmanis, 1998; Thompson et al., 2010) on timescales of minutes to days. The spatial distribution of vegetated and bare sites is thus a first-order control on the hydrology of these ecosystems. However, this spatial pattern changes slowly over time in response to drivers that include soil water availability, leading to a multiscale coupling of slow plant, and rapid hydrological, dynamics.

The tight but multiscale coupling of water and biological processes in drylands is necessary to sustain vegetation in areas where rainfall alone would not provide sufficient water for plant growth (Tongway and Ludwig, 2001). Loss of vegetation cover in drylands is known to risk irreversible desertification (Kéfi et al., 2007; Rietkerk et al., 2004). For the globally distributed suite of dryland ecosystems where vegetation forms regular spatial patterns (Bromley et al., 1997; Deblauwe et al., 2008; Penny et al., 2013), such ecological collapse may be preceded by changes in the spatial pattern of vegetation (HilleRisLambers et al., 2001; Rietkerk et al., 2002; Guttal and Jayaprakash, 2007; Gandhi et al., 2019).

Vegetation patterns occur when plants growing close together enhance each others growth (a facilitative interaction), while plants growing further apart inhibit each others growth (a competitive or inhibiting interaction) (Borgogno et al., 2009). Although numerous mechanisms are known to generate such facilitative and competitive interactions (Meron, 2015; Barbier et al., 2008), redistribution of overland runoff driven by the contrast in infiltration rates beneath plant canopies (Seghieri et al., 1997) and crusted or sealed bare soils (Belnap, 1990; Assouline, 2004) is a key process.

Modeling efforts to reproduce the morphology and sensitivities of banded vegetation (Rietkerk et al., 2004; Kéfi et al., 2007; van de Koppel et al., 2002; Rietkerk and Van de Koppel, 2008; Meron, 2016) must therefore confront the multiscale situation outlined above: fast hydrological processes that drive and are driven by slow plant growth and dispersal.

The physics of overland flow on landscapes with spatially varying surface roughness and infiltration capacity (i.e., patchily-vegetated landscapes), is best described by the Saint Venant equations (SVE) in two dimensions, also known as the shallow water equations (Thompson et al., 2011a; Crompton et al., 2020). These equations combine the continuity equation with conservation of momentum, and are illustrated here in their one dimensional form:

$$\frac{\partial h}{\partial t} + \frac{\partial}{\partial x}(Uh) = (p - i)\,, \tag{1}$$

$$\frac{\partial U}{\partial t} + U\frac{\partial U}{\partial x} + g\frac{\partial h}{\partial x} + g(S_f - S_o) + \frac{U}{h}(p - i) = 0, \tag{2}$$

where h is the water depth at location x and time t, U is the depth-averaged velocity, S_o and S_f are the bed- and friction- slopes, and g is the gravitational acceleration. Precipitation p and infiltration i are forcing terms that can vary with x and t.

Numerical solution of the SVE is computationally intensive. Studies that resolve the details of runoff and infiltration using the SVE or comparable physically-based models have therefore concentrated on individual storm events (Paschalis et al., 2016; Rossi et al., 2018; Chen et al., 2013). By contrast, models addressing the multiscale coupling of vegetation and water in patterned ecosystems overwhelmingly rely on simplifications of the flow equations, for example by approximating overland flow as a diffusive process, or approximating the intermittent occurrence of storms with continuous rainfall (Klausmeier, 1999; HilleRisLambers et al., 2001; Rietkerk et al., 2002), in order to render the long-term simulation of vegetation distributions computationally feasible.

Although the literature based on phenomenological flow models has had marked success in reproducing the phenomenology and morphology of vegetation pattern formation, the extent to which these phenomena can be related to climatic or land use 'thresholds' indicating degradation risk remains unclear. Quantitative predictions of the depth of cumulative infiltration during a storm and any subsequent runoff [hereafter, infiltration] remain quite distinct between the SVE and phenomenological models. This is illustrated in Figure 1, which compares infiltration predictions between the SVE and a typical phenomenological representation used in many patterned vegetation models: advective overland flow and depth-dependent infiltration dynamics (e.g. Rietkerk et al., 2002; Guttal and Jayaprakash, 2007, and related models). As shown in Figure 1, for a storm that produces nearly uniform infiltration through space in the phenomenological model, the SVE predicts a nearly binary set of low- versus high-infiltration zones that closely follow the vegetation distribution. These differences in predicted infiltration fields propagate into the predicted end-of-storm soil moisture distribution and subsequent vegetation growth, spread and mortality.

Many phenomenological models of hydrology in dryland ecosystems further limit the investigation of relationships between climate and pattern formation by simplifying the temporal properties of storms to continuous annual (Rietkerk et al., 2002), seasonal (Guttal and Jayaprakash, 2007) or daily rainfall fields, although several specific studies have relaxed these constraints (Kletter et al., 2009; D'Odorico et al., 2006; Siteur et al., 2014). Resolving the fast-timescale properties of storms is also important for accurately predicting infiltration fields (Crompton et al., 2019); the small runoff volumes generated in low-intensity storms infiltrate over short distances, leading to localized regions of elevated infiltration. By contrast, high-intensity storms generate runoff across the whole hillslope, resulting in more uniform infiltration fields within vegetated areas, as shown in supporting information Figure S1. Recently, Gandhi et al. (2019) used a timescale separation approach to simulate rainfall and storm responses on their appropriate timescales; however, this study retained a phenomenological representation of overland flow and infiltration.

This sensitivity of water distribution to storm properties creates a compelling need to improve the description of overland flow processes within multi-year simulations of dryland ecosystems. Here, we show that model emulation provides a way to reduce the numerical burden of simulating fast overland flow processes over many storm events, and thus a novel approach to increasing the numerical tractability of simulating multiscale systems.

Model emulation refers to a suite of approaches that replace a computationally-intensive process model with an accurate alternative model structure that is much faster to execute (Castelletti et al., 2012; Razavi et al., 2012; Rohmer et al., 2018). Although widely used in global climate modeling (Castruccio et al., 2014; Dueben and Bauer, 2018; Krasnopolsky and Fox-Rabinovitz, 2006; Raper and Cubasch, 1996) and finding new applications in groundwater and other earth science domains (Bhattacharjya and Datta, 2005; Broad et al., 2005; Castelletti et al., 2010; Kumar et al., 2010; Neelakantan and Pundarikanthan, 2000; Rogers and Dowla, 1994; Sreekanth and Datta, 2010; Yan and Minsker,

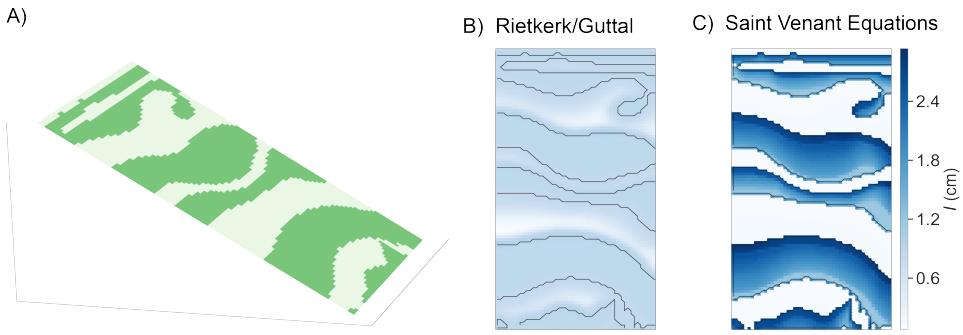

FIGURE 1 Illustration of the difference in storm-scale predictions between a phenomenological versus physical model. For the vegetation distribution in panel A, panels B and C show the infiltration distribution predicted by the R/G and SVE models for a single storm (with rain intensity $p = 2.4$ cm/hr and duration $t_r = 30$ min). The model parameters were 'matched' so that the infiltration capacity is a factor of 10 greater in vegetated areas than bare soil areas (in the R/G model, via the minimum surface water infiltration coefficient in the absence of plants, $W_o = 0.1$; in the SVE model, via the hydraulic conductivity ratio between vegetated and bare soil areas, $K_{S,B}/K_{S,V} = 0.1$). Other model parameters are given in Table 1 (for the R/G model) and Table 2 (for the SVE model), with the exception of the R/G effective slope parameter, $\nu = 10$ m/day and the rate of surface water infiltration, $\alpha = 30$ day^{-1}.

2003), emulation has not, to our knowledge, yet been applied to multiscale ecohydrological problems. Previously, we showed that predictions of overland flow and infiltration in patchily vegetated dryland systems made with a physical model (the Saint Venant Equations coupled to Richards Equation to describe infiltration) could be accurately emulated using a machine-learning method called random forest regression (Crompton et al., 2019).

In the present study, we use a similar emulation model to replace phenomenological descriptions of hydrological processes in a widely-used model of patterned dryland vegetation (Rietkerk et al., 2002; Guttal and Jayaprakash, 2007). By describing storm-scale runoff and infiltration processes, this replacement: (i) provides a proof-of-concept for the usefulness of emulation methods in multiscale environmental simulation, and (ii) enables an assessment of the sensitivity of pattern formation and morphology to storm properties and within-storm hydrological processes without recourse to phenomenological models. Using a physical model to represent the fast processes not only improves process fidelity, but allows for physically meaningful parameterization of the hydrological models and direct comparison of predictions to measured soil and climate properties.

2 | METHODS

The point of departure for the study is to integrate spatial infiltration fields predicted by a physical model of overland flow and infiltration into an existing pattern-forming vegetation model. The overland flow and infiltration processes are represented using the two-dimensional Saint Venant Equations coupled to Richards equation (the SVE model). The use of the SVE model allows hydraulically relevant features to be explicitly simulated, including contrasts in surface roughness and infiltration capacity between vegetated and bare areas (Istanbulluoglu and Bras, 2005; Smith et al., 2007; Thompson et al., 2010), the mean land surface slope, and realistic boundary conditions (no-flow boundary conditions at the hillslope divide and open boundary conditions at the valley floor, McGrath et al., 2011). Vegetation water use, growth and dispersal are modeled following Rietkerk et al. (2002), using the modifications made by Guttal and Jayaprakash (2007) (the R/G model). The models are coupled as the R/G-SVE model, as illustrated in Figure

2. Briefly, SVE model predictions of the end-of-storm spatial distribution of infiltration are used to update the soil moisture in the R/G framework; prior to each storm, the R/G model predictions of vegetation spatial pattern are then fed to the SVE model as boundary conditions. Details about the models and their coupling are provided in Sections 2.2 and 2.3.

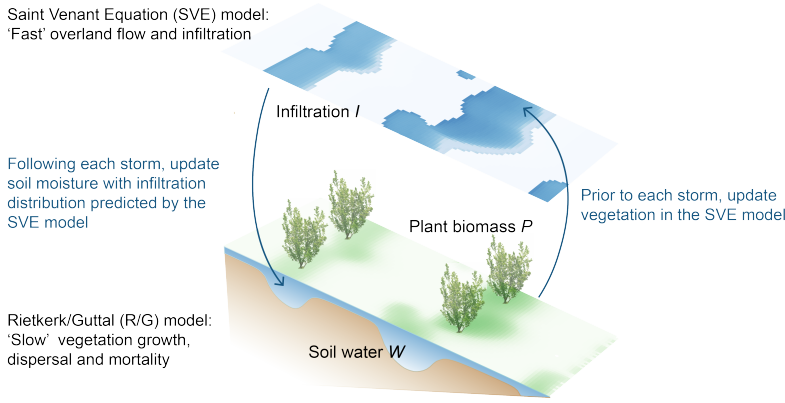

FIGURE 2 Illustration of the approach used to couple the R/G and SVE models. Following each storm, the pre-storm soil water field W is updated with the infiltration field I predicted by the SVE model. Between storms, plant biomass P and soil moisture W are described by the R/G model, with zero infiltration. Prior to each storm, the R/G biomass distribution is fed to the SVE model. Blue colors on the simulated landscape represent the soil water resource availability, and green colors the biomass density.

Next, the model framework is duplicated using a machine-learning based emulator to replace the SVE model predictions (the R/G-emulator model), as described in Section 2.4. To test the suitability of the R/G-emulator to replace the R/G-SVE, both models - R/G-SVE and R/G-emulator - are used to predict the same climate and vegetation conditions for a constrained range of storm climatologies. The predictions from each model are compared in terms of pattern morphology and sensitivity to different storm properties, as described in Section 2.5. Finally, the R/G-emulator model is used to assess the sensitivity of pattern morphology to within-storm characteristics over a large range of rainfall climatologies in Section 2.6. The project workflow is illustrated schematically in Figure 3.

2.1 | The Saint Venant - Richards Equation model

The Saint Venant-Richards Equation (SVE) model couples a finite volume solver for the two-dimensional Saint Venant Equations (Bradford and Katopodes, 1999) to a one-dimensional (vertical) Richards equation model for infiltration (Celia et al., 1990). The resulting model, including validation against analytical solutions, is described in more detail in Crompton et al. (2019) and Crompton et al. (2020). Throughout this study, land surfaces were simulated as planar hillslopes with a fixed slope gradient. No-flow boundary conditions were applied at the divide, and flow exiting the bottom of the slope was assumed to leave the domain. To address spatial variations in infiltration and roughness in the patchily vegetated landscape, the landscape was binarized into 'bare' or 'vegetated' patches based on the modeled biomass field. This binarization assumes that it is the presence or absence of vegetation that most determines spatial variations in these properties, a reasonable assumption in many dryland landscapes (Thompson et al., 2010). A plant biomass $P(x, y, t)$ threshold of $P_T = 20$ g/m^2 was used to separate bare and vegetated sites. Typical soil and

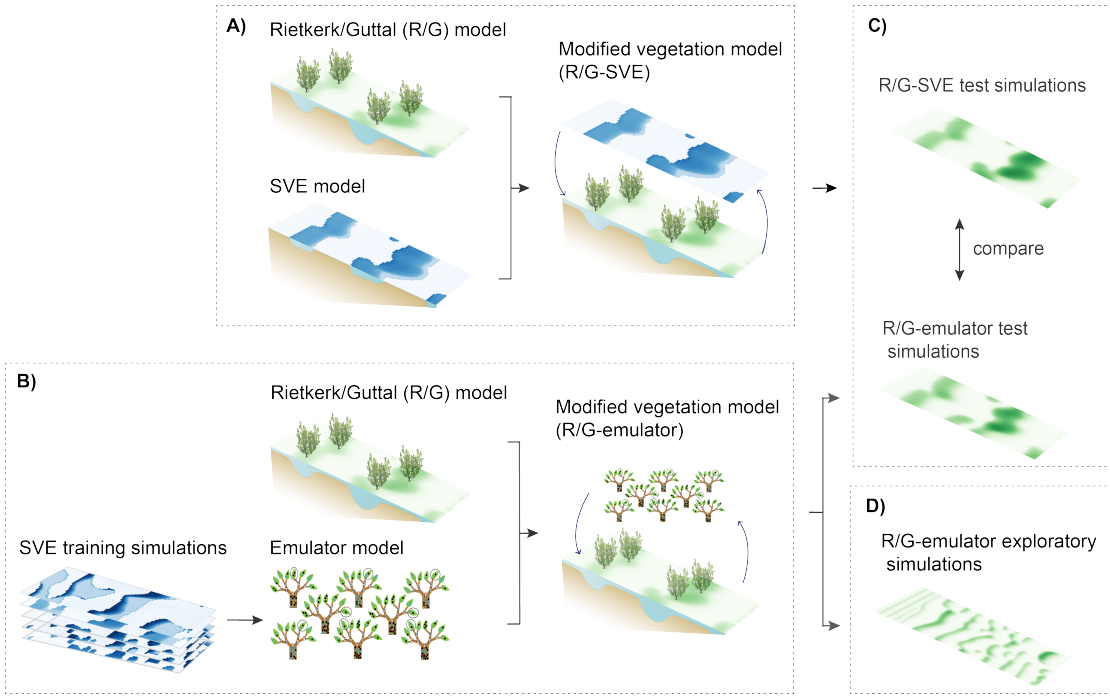

FIGURE 3 Steps involved in constructing and testing the modified vegetation model. (A) The R/G model was coupled to the SVE model as the 'R/G-SVE model'. (B) The R/G model was coupled to the SVE emulator model as the 'R/G-emulator model', which emulates the R/G-SVE model predictions. (C) To assess the R/G-emulator model performance, the R/G-SVE and R/G-emulator models were run for identical initial conditions, storm climatologies and vegetation parameters (the 'test simulations'). (D) The R/G-emulator model was used to explore a range of annual rainfall amounts R, on a larger hillslope domain.

roughness values observed in patterned vegetation sites (Tongway and Ludwig, 1990; Bromley et al., 1997; Dunkerley, 2002; Thompson et al., 2010) were used to parameterize the SVE model. Enhanced infiltration rates in vegetated patches were represented by a 10:1 K_{sat} ratio (K_{sat} = 1.5 and 0.15 cm/hr in vegetated and bare sites). Throughout, infiltration capacity was treated as a constant rate, and approximated as K_{sat}. Surface roughness was parameterized with Manning's equation, with n = 0.1 and 0.03 in vegetated and bare sites, respectively. All simulations used a 200×100 m hillslope domain with a slope gradient of 2%. Complete SVE model parameters are further defined in the following sections and listed in Table 2.

2.2 | The Rietkerk/Guttal pattern-forming model

The selected vegetation model was proposed by Rietkerk et al. (2002) and modified by Guttal and Jayaprakash (2007). The Rietkerk-Guttal (R/G) model consists of three spatially-explicit, coupled partial differential equations that describe dynamics of the plant biomass density (P; g m^{-2}), the local depth of water stored within the soil (W; mm), and the local depth of ponded water on the land surface (O; mm), as shown below:

$$\frac{\partial O}{\partial t} = r - \alpha O \frac{P + W_0 k_2}{P + k_2} + \nu \frac{\partial O}{\partial x} \tag{3}$$

$$\frac{\partial W}{\partial t} = \alpha O \frac{P + W_0 k_2}{P + k_2} - g_{max} \frac{W}{W + k_1} P - r_w W + D_w \nabla^2 W \tag{4}$$

$$\frac{\partial P}{\partial t} = \frac{1}{\tau_p(W)} \left(c g_{max} \frac{W}{W + k_1} - d \right) P + D_p \lambda^2 P \tag{5}$$

where

$$\frac{1}{\tau_p(W)} = \frac{1}{4} \frac{W^2 + f k_3^2}{W^2 + k_3^2} \tag{6}$$

The $\frac{1}{\tau_p(W)}$ term was introduced by Guttal and Jayaprakash (2007) to account the persistence of dryland vegetation throug long periods of limited soil water. The modification slows the rates of biomass growth and decay while soil moisture is limited, reflecting drought-adaptations in desert vegetation. The model forms a broad suite of vegetation patterns and is the basis for an extensive modeling literature exploring the dynamics of these patterns (Baartman et al., 2018; Dagbovie and Sherratt, 2014; Gandhi et al., 2019; Pueyo et al., 2008; Saco et al., 2007).

The biological parameters in the R/G model simulations were selected following Guttal and Jayaprakash (2007) and held constant for all simulations. The parameters (including their definitions, units and values used) are listed in Table 1.

2.3 | Incorporating storm-scale infiltration in the R/G model

The R/G model simplifies hydrological processes by (i) representing overland flow velocities as advection, and (ii) depicting infiltration capacity as a function of biomass and ponded water depth, rather than as a function of local soil properties and the duration of soil inundation. As shown previously in Figure 1, these simplifications can lead to large discrepancies between its predictions of the spatial field of water availability and those predicted with the SVE. To avoid these discrepancies, the modeled biomass field P is used as input to the SVE model for a given storm, where it determines the spatial pattern of soil hydraulic and roughness properties as outlined in Section 2.1. The SVE predictions of infiltration depth for the storm ($I_{storm}(x, y, t)$) are converted to a rate (i_{storm}) based on the R/G model timestep ($i_{storm} = I_{storm}/dt$), and replaces the infiltration term in Equation 4 ($\alpha O \frac{P+W_0 k_2}{P+k_2}$). With this modification, Equation 4 becomes:

$$\frac{\partial W}{\partial t} = i_{storm} - g_{max} \frac{W}{W + k_1} P - r_w W + D_w \nabla^2 W \tag{7}$$

where $i_{storm} = 0$ between storms by definition. Replacing the surface water equation with SVE predictions of infiltration introduces physically interpretable landscape parameters, such as the hillslope gradient S_o and soil hydraulic

TABLE 1 Model parameters, descriptions and values for the Rietkerk/Guttal component of the coupled R/G-emulator and R/G-SVE models. Several variables from Guttal and Jayaprakash (2007) have been replaced by our use of the SVE model. Parameter values that differ from those used in Guttal and Jayaprakash (2007) are noted with an asterisk.

Parameter	Description	Units	Values
c	Conversion factor for water uptake to plant biomass	g m^{-2} mm^{-1}	5
g_{max}	Maximum specific water uptake	mm $g^{-1} m^{-2} day^{-1}$	0.1
k_1	Half-saturation constant of specific plant growth and water uptake	mm	5
m	Specific rate of plant density loss due to mortality	day^{-1}	0.25
r_w	Soil water loss rate due to evaporation and drainage	day^{-1}	0.4
k_3	Soil water scale at which plant growth resumes normal metabolic activity	mm	10
f	Metabolic activity coefficient at zero water availability	–	0.04
D_p	Plant dispersal diffusion constant	m^2 day^{-1}	0.02*
D_w	Soil water diffusion constant	m^2 day^{-1}	0.1
Other parameters			
$\phi_{V,0}$	Initial fractional vegetation cover	–	0.5
P_T	Threshold biomass	g m^{-2}	20.
R/G model parameters that are replaced by SVE predictions			
α	Rate of surface water infiltration	day^{-1}	–
k_2	Plant density scale determining how surface water infiltration increases with P	g m^{-2}	–
W_0	Minimum surface water infiltration coefficient in the absence of plants	–	–
v	Effective slope parameter	m day^{-1}	–
r	Daily rainfall rate	mm day^{-1}	–

parameters (e.g., saturated hydraulic conductivity, K_{sat}), as well as temporally resolved storm parameters, such as the intensity, duration and between-storm interval. Following the storm, the biomass and soil water fields evolve according to the equations in the original R/G model.

The R/G-SVE model enables assessment of the impacts of different rainfall volumes and intensities on pattern morphology. To simplify this assessment, we used idealized rainfall time-series consisting of identical discrete storms occurring on equal intervals year round. This approach eliminates seasonality and stochasticity in the timing and magnitude of storms, but provides a tractable starting point to assess the impacts of storm properties on vegetation patterns. Sixteen unique storms were formed by combining four rainfall depths (d = 0.4, 0.8, 1.2, 1.6 cm per storm) and four durations (t_r = 10, 20, 30, 40 minutes), resulting in eleven unique rainfall intensities ($p = d/t_r$). We fixed the storm characteristics and specified the waiting interval τ between storms to generate a range of annual rainfall volumes R ($R = 365d/\tau$). This approach allowed us to treat d, t_r and R as independent variables specifying different storm climatologies. Together, d and R determine τ, and d and t_r determine the rainfall intensity p.

For consistency with the domain represented by the SVE model, we did not impose periodic boundary conditions in the R/G model (a departure from Rietkerk et al. (2002) and Guttal and Jayaprakash (2007)). Instead, the modified R/G model implements a zero-flux boundary at the hillslope divide. Because of the well-known tendency for vegetation bands to migrate uphill with time (Thompson and Katul, 2009), the downslope boundary of the R/G model was 'seeded' at each storm event with a random biomass distribution (identical to that used to initialize the simulations).

TABLE 2 Parameters for the SVE model, as used in (i) the SVE simulations required to train the emulator model, and (ii) the coupled R/G-SVE model simulations. Simulations were run for all 16 combinations of storm parameters, t_r and d. Note that to represent the effects of vegetation on the flow hydraulics: K_{sat} = 1.5 cm/hr in vegetated sites and K_{sat} = 0.15 cm/hr in bare soil areas; flow resistance is parameterized with Manning's equation, with n = 0.1 in vegetated areas and n = 0.03 in bare soil areas.

Parameter	Description	Units	Values
	Storm parameters		
t_r	Storm duration	min	10, 20, 30, 40
d	Storm depth	cm	0.4, 0.8, 1.2, 1.6
	Domain parameters		
n_I	Manning's n (impermeable)	s $m^{-1/3}$	0.03
n_P	Manning's n (permeable)	s $m^{-1/3}$	0.1
L_x, L_y	Domain size	m	200×100
dx	Grid resolution	m	2.0
S_o	Hillslope gradient	%	2.0
	Soil parameters		
$K_{S,V}$	Hydraulic conductivity (vegetated areas)	cm/hr	1.5
$K_{S,B}$	Hydraulic conductivity (bare soil areas)	cm/hr	0.15
s	Pore size distribution	–	1.47
α	van Genuchten parameter	–	9.6e-3
θ_S	Saturated soil moisture content	–	0.472
θ_R	Residual soil moisture content	–	0.0378
z_{max}	Soil depth	cm	20.0
H_0	Initial H	cm	-342.0

2.4 | Emulation of the SVE model with machine learning

Crompton et al. (2019) used machine learning (random forest regression of SVE output) to rapidly predict the spatial distribution of storm-scale infiltration following runoff generation and infiltration on a patchily-vegetated domain. The emulator predicts infiltration for every location on a hillslope with an arbitrary spatial pattern of vegetated and bare sites but fixed soil, slope, and storm properties (see Figure 4). To apply random forest regression to spatial data, the spatial vegetation fields are simplified as a collection of univariate metrics or 'features'. Each point is mapped to a feature array that describes the cell type (bare or vegetated), the spatial distribution of neighboring vegetated and bare soil cells, and the distance to the divide. Examples of features include, for vegetated cells, the distance to the nearest upslope bare soil area and the length of the upslope bare soil area. A complete list of features, and code to compute these features for an input vegetation field, are available at CUAHSI Hydroshare (Crompton, 2020).

As the relationships between vegetation pattern and infiltration depth are not stationary across varying storm characteristics, a separate random forest is trained for each unique storm (i.e., combinations of d and t_r described above). Thus, the present study involved 16 random forests, which together form the emulator. Each individual random forest was trained on a collection of multiple SVE simulations consisting of multiple vegetation spatial patterns, with storm characteristics held constant. To adapt the emulation approach to the present application, the random forests were trained on a broader set of features than in Crompton et al. (2019) and on more training patterns, including 20 patterns typical of banded vegetation.

A comprehensive test of the original emulator is provided in Crompton et al. (2019), and was not repeated in the present study. The emulation approach was implemented with minor modifications, and to check that the performance was acceptable, we assessed the training and test errors using: (i) the SVE simulations used to train the emulator, and (ii) SVE simulations extracted from the R/G-SVE model simulations. The fidelity with which the emulator reproduced the within-hillslope spatial patterns was estimated the normalized root mean square error (NRMSE) between the SVE and emulator predictions:

$$\mathrm{NRMSE} = \frac{1}{d}\sqrt{\frac{1}{N_{cell}}\sum_{N_{cell}}\left(I - I_{RF}\right)^2} \tag{8}$$

where I is the SVE model prediction, I_{RF} is the emulator prediction, d is the storm depth, and summation over N_{cell} is over all of the points in the hillslope domain. The median and standard deviation of the errors was 2.7 ± 2.2 % for the training set and 5.3 ± 6.0 % for the test set, which is similar to the original analysis.

2.5 | Testing of the R/G-emulator model

Comparisons of the output from paired R/G-SVE and R/G-emulator model runs were used to test the R/G-emulator model. The test cases had the same annual rainfall $R = 438$ mm, but were generated using sixteen different storm climatologies, consisting of all combiantions of the four storm depths d and four storm durations t_r described above, with the wait intervals adjusted to hold annual rainfall constant. Each of the paired R/G-SVE and R/G-emulator model simulations was run for 632 storms. Because wait intervals varied between the storms, the final length of the simulations ranged between 2096 and 8398 days. The R/G-SVE model was expensive to run: 632 storm events required approximately 2 months of supercomputer time. For this reason, we did not extend the length of the simulations or the range of climatologies, but verified that the simulations were approaching steady state (see supporting information Figure S2-S4), allowing a reasonable comparison of the R/G-SVE and R/G-emulator models at this time. These

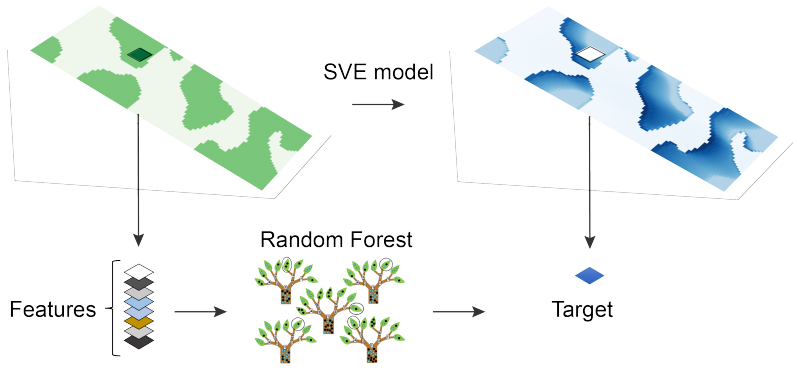

FIGURE 4 The hillslope on the left shows a sample distribution of vegetation, and the hillslope on the right shows an SVE model prediction of infiltration depth, representing the target variable. Each point in the SVE model domain is transformed into a 1D vector of features that represent the surrounding neighborhood. The random forest independently operates on each point to predict the outcome.

computational limitations also prevented us from a comprehensively characterizing uncertainty; for example, we did not explore how deviations between R/G-emulator and R/G-SVE predictions varied with initial condition.

We used three metrics of pattern morphology to characterize the differences between the R/G-SVE and R/G-emulator simulations: (i) the number of bands within the domain, (ii) within-patch mean biomass P_{patch} (g/m^2), and (iii) vegetation fraction ϕ_V (the fraction of the domain occupied by vegetated sites). The number of bands within the domain, determined by counting the number of repeated vegetation-bare soil units along the hillslope length, is a proxy for pattern wavelength, and is a more robust metric than a true wavelength (identified, e.g. via peaks in a power-spectrum) for simulations where the wavelength approached or exceeded the model domain length. To define P_{patch} and ϕ_V, a biomass threshold of $P_T = 20$ g/m^2 was used to delineate vegetated from bare sites. All metrics were computed for each along-slope column on the modeled hillslope, and aggregated.

Figure 5A presents paired violin plots that compare the R/G-SVE and R/G-emulator model predictions of band count, P_{patch} and ϕ_V for each storm climatology, with the storms sorted in order of increasing rainfall intensity. A comparison of the blue (emulator) and grey (SVE) metrics shows that, in general, there is good agreement between the model versions, although the SVE predictions often show more across-slope variation relative to the emulator. Additionally, the sensitivity of the pattern properties to storm intensity is preserved between the models; the band count decreases and within-patch biomass increases with increasing rainfall intensity for both model approaches. The results suggest that the emulation approach reproduces vegetation pattern morphologies, and their sensitivities to storm climatology, relative to the SVE approach. Panels B and C in Figure 5 show example side-by-side comparisons of the R/G-SVE and R/G-emulator predictions of the spatial distributions of biomass at the end of the simulations for two storm climatologies. Similar comparisons for all sixteen storms are provided as supporting information Dataset S1. Hillslope-averaged summary metrics and errors are reported in supporting information Table S1.

2.6 | Exploratory simulations with the R/G-emulator model

Using the emulator model to predict infiltration sped up the prediction by a factor of >10,000 , enabling exploration of the sensitivity of pattern morphology to storm characteristics under varying climate aridity and on a larger hillslope domain of length 400 m and width 200 m. For each of the sixteen storm types, annual rainfall intensity R was varied

between 219 and 511 mm, again by adjusting the wait interval between storms. All simulations were run to 10,000 days.

3 | RESULTS

Figure 6 illustrates the range of pattern morphologies generated by the sixteen storm types for a common annual rainfall of $R = 292$ mm, illustrating the potential for storm properties to influence pattern morphology. With annual rainfall held constant, the pattern morphology varies from a nearly-bare state, to fragmented vegetation conditions, to coherent banded patterns with a range of wavelengths.

Figure 7 summarizes the sensitivity of the pattern spatial metrics to changes in annual rainfall and storm intensity (increasing from left to right, where climatologies with the same intensity are grouped with vertical lines). In this plot, some rainfall climatologies do not result in the formation of a vegetation pattern. In some low-intensity cases with $R \geq 365$ mm, biomass cover is continuous and the vegetation cover is effectively homogeneous. Similarly, in some high-intensity cases with $R \leq 365$ mm, minimal biomass is sustained (i.e. <5 g/m^2) and the patterns collapse. Based on visual inspection, we required that the standard deviation of the biomass field, std(P), be greater than 7.0 g/m^2 for the result to be considered a 'pattern' (see supporting information Figure S5 for visual comparisons of biomass fields immediately above and below this threshold).

Several broad trends can be identified in Figure 7: increasing rainfall intensity is generally associated with decreasing band count (panel A) and increasing P_{patch} (panel C). The vegetation fraction does not exhibit clear trends with rainfall intensity, but increases on average with increasing annual rainfall. Figure 7 suggests that desertification is not only associated with lower annual rainfall R (note the greater number of 'missing' data points for $R = 219$ mm than for higher annual rainfall cases), but also promoted by increasing rainfall intensity - presumably because more rainfall runs off and is lost from the hillslope as intensity increases. This is illustrated in supporting information Figure S6 with a sample vegetation pattern. Additional examples of desertification due to increasing rainfall intensity are shown in supporting information Figures S7-S8 (for R = 219 - 292 mm). At higher annual rainfall totals, missing data in Figure 7 are associated with homogeneous vegetation cover (see supporting information Figures S10-S11, for R = 483 - 511 mm). For R = 365 mm, patterns form for all 16 storm scenarios, as shown in supporting information Figures S9.

While Figure 7 highlights the clear dependence of pattern band count and P_{patch} on rainfall intensity, intensity alone does not determine the pattern morphology. For example, in Figure 6, intensity is constant along the upper-left to lower-right diagonal ($p = 2.4$ cm/hr); however, from smaller, more frequent storms (d= 0.4 cm) to larger, less frequent storms (d = 1.6 cm), pattern wavelengths and bandwidths increase, while pattern 'coherency' appears to decrease. Similar dependencies of morphology on d can be seen for $p = 2.4$ cm/hr in Figure 7.

The results suggest that the conditions for pattern formation in these simulations vary in a complex fashion with total annual rainfall and within-storm characteristics. The generalization that pattern formation and morphology is sensitive to annual rainfall, widely identified in previous studies (Rietkerk et al., 2002; Guttal and Jayaprakash, 2007) is repeated here: band count decreases and within-patch biomass increases with increasing annual rainfall inputs (see e.g., supporting information Figures S12-S15). However, as is also evident in supporting information Figures S12-S15, the range of annual rainfalls over which patterns form depends on storm characteristics.

4 | DISCUSSION

The results demonstrate how the redistribution of water as surface runoff during storms, and the sensitivity of this redistribution to storm properties such as intensity and duration, propagates and influences pattern morphology on ecological timescales. Although the annual rainfall sets a broad trend in vegetation fraction within the simulations, the organization of this vegetation into patchy landscapes of varying morphologies and biomass densities is sensitive to storm-scale runoff-runon processes, and thus to the storm duration and intensity. Whereas previous research into the connections between vegetation spatial organization and desertification focused on declining annual rainfall, these simulations indicate that increased storm intensity could be sufficient to degrade landscapes, even if total annual rainfall is constant. This finding is consistent with Siteur et al. (2014), who found that, for a constant annual rainfall rate, an increase in storm intensity can trigger desertification as a greater fraction of the rainwater is lost as runoff. This is significant because many climate projections predict increased intra-annual rainfall variability, characterized by fewer yet larger, more intense rainfall events and longer dry spells (Giorgi et al., 2011; Kharin et al., 2013; Westra et al., 2014; Prein et al., 2017), exactly the scenario associated with desertification in the simulations here. In the modeling framework presented here, rainfall intensity is tightly coupled to runoff production and increasing rainfall intensity reduces the fraction of rainfall that can infiltrate on a given hillslope. Additionally, and absent from these simulations, greater rainfall intensity and runoff velocities promote surface erosion, which can powerfully accelerate degradation and desertification (Watson and Laflen, 1986; Römkens et al., 2002).

The present study is limited in scope to rainfall with fixed intervals between identical showers of constant intensity. However, the proposed framework is well suited to investigate the effects on vegetation patterns of rainfall seasonality, stochasticity, intermittency and intensity, topics which have been previously examined with phenomenological treatments of storm-scale processes (Gandhi et al., 2019; Ursino and Contarini, 2006; Kletter et al., 2009; Baudena et al., 2013; D'Odorico et al., 2006). Indeed, the model modifications that would be necessary to explore rainfall seasonality, intermittency and stochasticity are trivial, namely, adjusting the wait intervals between storm events. Integrating a more realistic range of storm intensities and durations (e.g., following an intensity-duration-frequency curve) would require training additional SVE emulators for each unique storm, also a minor modification.

In addition to better identifying the connections between rainfall processes and desertification risk, this study highlights the difficulties associated with attempting to directly link the morphology of vegetation patterns to environmental drivers. Previous studies have attempted to interrogate or invert models of vegetation pattern formation to gain insight into dryland ecosystem function and improve predictions about their resilience (Penny et al., 2013; Thompson and Katul, 2011; Mander et al., 2017), or to improve the process realism of patterned vegetation models without addressing within-storm processes (Kefi et al., 2008; Thompson and Katul, 2009; Vincenot et al., 2016). In part, these efforts aimed to improve the ability to compare observed and modeled patterns (Dunkerley, 2018; Barbier et al., 2014, 2008). The present study, however, highlights that unless models address the multiscale nature of dryland ecohydrology, sensitivity to storm-scale processes (and the omitted issues of seasonality and stochasticity among storm events) may confound such efforts (Guttal and Jayaprakash, 2007; Deblauwe et al., 2008; Vincenot et al., 2016; Gandhi et al., 2019).

A valid question remains whether other water related parameters in the R/G model (e.g. the advection and infiltration parameters) could be tuned to "map" the pattern morphologies between the R/G-emulator and the original R/G model for a given annual rainfall - i.e., adjusting these parameters to account for the errors involved in neglecting storm-scale processes. Although we have not comprehensively explored this possibility, our preliminary attempts to map the pattern morphologies between the models were not encouraging, as the pattern-forming regions of parameter space appear to be disparate between model versions (Crompton, 2018). The difficulties associated with this

mapping also meant that we did not attempt to compare our predictions to phenomenological predictions, as it is unclear how to meaningfully parameterize these models to represent the same landscape and climate as explicitly defined in the SVE model.

Beyond the case study of vegetation patterns, coupling the emulator and pattern-forming models provides a proof of concept of the usefulness of emulation methods for making multiscale ecohydrological predictions. This study has demonstrated the feasibility of this approach, and the potential value of emulation modeling in revealing dynamics that arise from multiscale interactions that were previously unexplored in the study system. While the patterns generated by the R/G-SVE and R/G-emulator models exhibit small differences, changetheir predictions of thethe simulated pattern morphologies and biomass distributions, and their sensitivities to storm characteristics, are similar between model versions. The differences between the R/G-SVE and R/G-emulator model predictions are likely attributable to the strongly nonlinear pattern-forming model - such nonlinearities are known to amplify small differences in initial conditions, and likely also amplify the effects of small errors in the emulated infiltration fields.

The study was also subject to several computational considerations that could be improved upon by future researchers, relating to: (i) the numerical demands of validating the use of emulation approaches in coupled multiscale models, and (ii) the computational sophistication needed to implement the workflow that was used in this study. Most pressingly, the use of the emulation within the multiscale model required assessment of how errors in the emulator model propagated through the pattern-forming model. Unavoidably, such an assessment requires that researchers undertake the very task that the use of an emulator model seeks to avoid - the coupling of the computationally-intensive process model with the pattern-forming model. In this case, over 600 SVE model runs were needed per validation case, approximately 2 months of supercomputer time. The situation is a little paradoxical: as the computational demands of the physical model increase, the use of emulation modeling becomes both more urgent and more expensive to validate. In cases where the slow processes are more linear than in the present case, validation may be less problematic, as such models are less likely to amplify small errors than the pattern-forming vegetation model. However, this study illustrates the trade-offs between the numerical expense of validation, the required quality of uncertainty characterization, and the numerical benefits of using an emulation approach at all.

Secondarily, the required workflow is non-trivial, involving (i) creating a library of physical model simulations upon which to train the emulator model for the fast processes, (ii) coupling the physical and emulator models to the 'slow' model, (iii) running both versions of the resulting multiscale model to validate the emulator version, and (iv) making predictions with the final (emulation-based) multiscale model. Implementing this workflow requires significant time investments in data organization, data storage, and coding, and the value of such investments for one-off applications is questionable. Creating virtual and model-independent environments that could support such workflows in the future (similar to those developed already to support e.g., uncertainty characterization or data assimilation (Anderson et al., 2009; Welter et al., 2015)) could lower this burden and increase the accessibility of emulation methods for multiscale modeling.

5 | CONCLUSION

This study illustrated how emulation modeling can provide a viable pathway towards including greater process complexity within ecohydrological models that contain a strong timescale separation between interdependent processes. By replacing a phenomenological representation of overland flow and infiltration processes with a machine-learning emulation of a surface hydrological model, we were able to introduce within-storm processes to vegetation pattern-forming systems without compromising model runtime.

The patterns produced by the emulator version were sufficiently similar to those produced by the physical version to enable the exploration of a larger parameter space of annual rainfall amounts, over a larger domain size. We were able to demonstrate the sensitivity of pattern morphology to storm properties; specifically, increased storm depths and reduced storm durations were associated with longer wavelengths (smaller band counts) and greater within-patch biomass. In dry climates (i.e. those with lower annual rainfall totals), the pattern morphology was also sensitive to increased intensity and lower frequency storms, fragmenting from bands to spots to non-vegetated states. No similar behavior can be produced with the R/G model without representing storm properties.

Given that ecohydrological processes by their nature embrace complex biological and physical coupling across multiple spatial and timescales, we suggest that emulation approaches deserve broad consideration to address the computational challenges associated with representing such diverse multiscale phenomena.

6 | ACKNOWLEDGEMENTS

OC and SET acknowledge funding from the National Science Foundation (NSF) grant numbers NSF-EAR-BSF 1632494 and NSF-EAR-1555041. We thank SF Bradford and ND Katopodes for providing the code for the SVE solver described in Bradford and Katopodes (1999).

7 | DATA AVAILABILITY

This manuscript relied only on model output generated by the authors during the course of the study. The code and simulation data that support the findings of this study are openly available at CUAHSI HydroShare at: http://www.hydroshare.org/resource/0db36216de7a42bf90de89b901ca6102

8 | CONFLICT OF INTEREST

The authors have declared no conflicts of interest for this article.

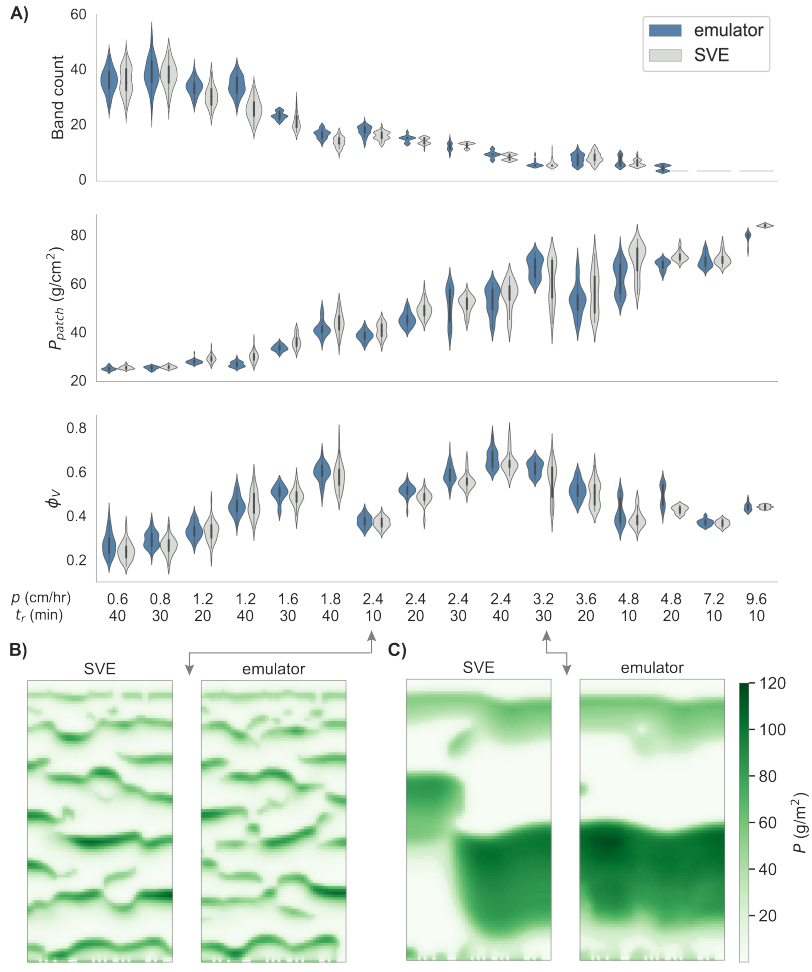

FIGURE 5 Test simulation results, comparing the R/G-SVE and R/G-emulator model predictions. Panel A shows side-by-side violin plots for the three metrics of pattern morphology. From top to bottom, these metrics are band count, the mean within-patch biomass P_{patch}, and the vegetation cover fraction ϕ_V. The x-axis on each plot shows each distinct storm scenario in terms of intensity p and storm duration t_r, and storms are ordered from left to right with increasing p. Panels B and C show side-by-side comparisons for two storm climatologies with good and poor agreement between models, respectively (B: t_r = 10 min, d = 0.4 cm; and C: t_r = 30 min, d = 1.6 cm).

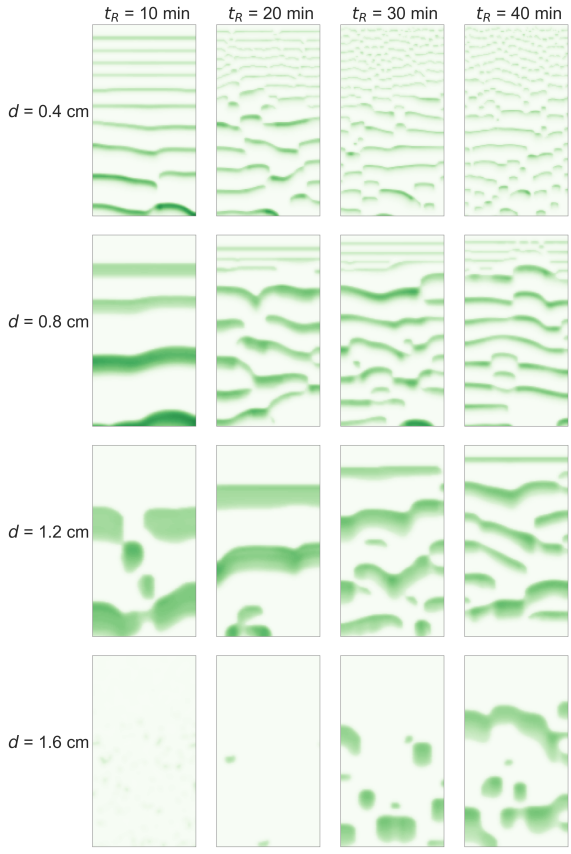

FIGURE 6 R/G-emulator model predictions of pattern morphologies after 10,000 days, with annual rainfall fixed at $R = 292$ mm. The subplots are organized with rainfall intensity decreasing from left to right, and increasing from top to bottom. Pattern morphologies for the other annual rainfall cases are included in supporting information Figures S7-S11. The color scale is the same between subplots and ranges from 0 g/m^2 (white) to 120 g/m^2 (green).

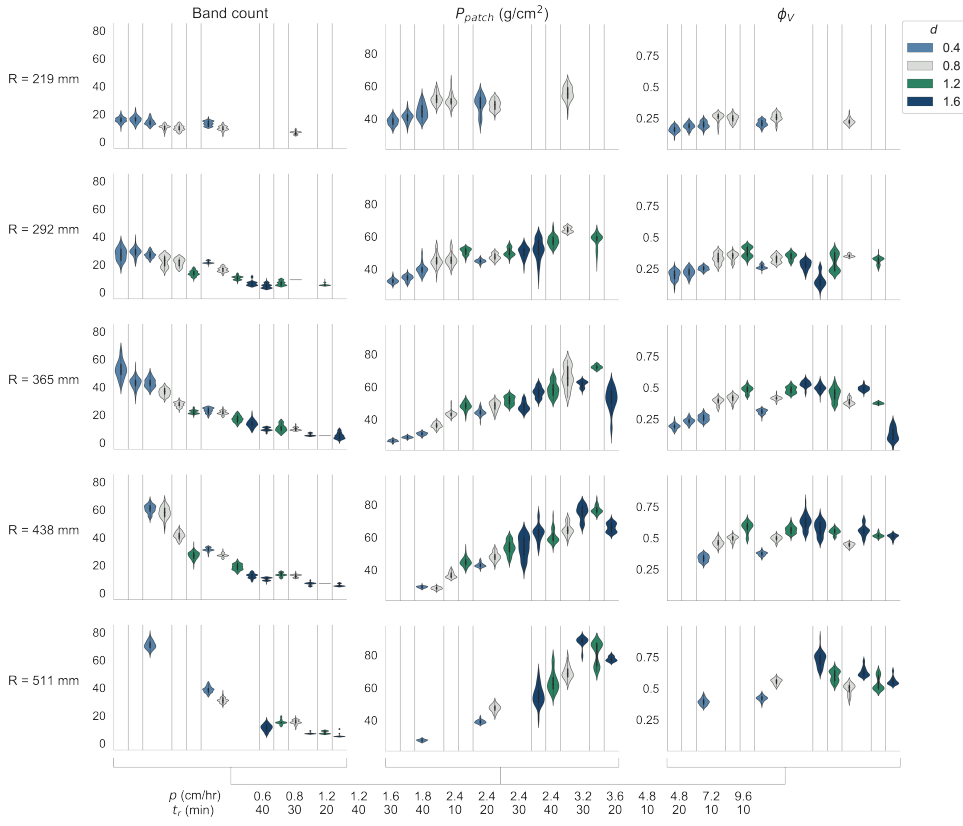

FIGURE 7 Summary of the sensitivity of pattern morphology to storm climatology. The violin plots in each column are sorted in order of increasing rainfall intensity (as in Figure 5), with colors indicating the rain depth. Because the same rainfall intensities appear multiple times (for different combinations of rainfall duration t_r and depth d), vertical lines are used to group the results associated with storms of equal intensity. The homogeneous and desertified cases are shown as blanks.

references

Anderson, J., T. Hoar, K. Raeder, H. Liu, N. Collins, R. Torn, and A. Avellano
2009. The data assimilation research testbed: A community facility. *Bulletin of the American Meteorological Society*, 90(9):1283–1296.

Assouline, S.
2004. Rainfall-induced soil surface sealing. *Vadose Zone Journal*, 3(2):570–591.

Baartman, J. E., A. J. Temme, and P. M. Saco
2018. The effect of landform variation on vegetation patterning and related sediment dynamics. *Earth Surface Processes and Landforms*, 43(10):2121–2135.

Barbier, N., P. Couteron, and V. Deblauwe
2014. Case study of self-organized vegetation patterning in dryland regions of central africa. In *Patterns of land degradation in drylands*, Pp. 347–356. Springer.

Barbier, N., P. Couteron, R. Lefever, V. Deblauwe, and O. Lejeune
2008. Spatial decoupling of facilitation and competition at the origin of gapped vegetation patterns. *Ecology*, 89(6):1521–1531.

Baudena, M., J. von Hardenberg, and A. Provenzale
2013. Vegetation patterns and soil–atmosphere water fluxes in drylands. *Advances in water resources*, 53:131–138.

Belnap, J.
1990. Microbiotic crusts: their role in past and present ecosystems. *Park Science*, 10(3):3.

Bhattacharjya, R. K. and B. Datta
2005. Optimal management of coastal aquifers using linked simulation optimization approach. *Water resources management*, 19(3):295–320.

Blöschl, G. and M. Sivapalan
1995. Scale issues in hydrological modelling: a review. *Hydrological processes*, 9(3-4):251–290.

Borgogno, F., P. D'Odorico, F. Laio, and L. Ridolfi
2009. Mathematical models of vegetation pattern formation in ecohydrology. *Reviews of Geophysics*, 47(1).

Bradford, S. F. and N. D. Katopodes
1999. Hydrodynamics of turbid underflows. i: Formulation and numerical analysis. *Journal of hydraulic engineering*, 125(10):1006–1015.

Briggs, G. E. and J. B. S. Haldane
1925. A note on the kinetics of enzyme action. *Biochemical journal*, 19(2):338.

Broad, D. R., G. C. Dandy, and H. R. Maier
2005. Water distribution system optimization using metamodels. *Journal of Water Resources Planning and Management*, 131(3):172–180.

Bromley, J., J. Brouwer, A. Barker, S. Gaze, and C. Valentine
1997. The role of surface water redistribution in an area of patterned vegetation in a semi-arid environment, south-west niger. *Journal of Hydrology*, 198(1-4):1–29.

Castelletti, A., S. Galelli, M. Ratto, R. Soncini-Sessa, and P. C. Young
2012. A general framework for dynamic emulation modelling in environmental problems. *Environmental Modelling & Software*, 34:5–18.

Castelletti, A., F. Pianosi, R. Soncini-Sessa, and J. Antenucci
2010. A multiobjective response surface approach for improved water quality planning in lakes and reservoirs. *Water Resources Research*, 46(6).

Castruccio, S., D. J. McInerney, M. L. Stein, F. Liu Crouch, R. L. Jacob, and E. J. Moyer
2014. Statistical emulation of climate model projections based on precomputed gcm runs. *Journal of Climate*, 27(5):1829–1844.

Celia, M. A., E. T. Bouloutas, and R. L. Zarba
1990. A general mass-conservative numerical solution for the unsaturated flow equation. *Water resources research*, 26(7):1483–1496.

Chen, L., S. Sela, T. Svoray, and S. Assouline
2013. The role of soil-surface sealing, microtopography, and vegetation patches in rainfall-runoff processes in semiarid areas. *Water Resources Research*, 49(9):5585–5599.

Crompton, O.
2020. Sensitivity of dryland vegetation patterns to storm characteristics, HydroShare. `http://www.hydroshare.org/resource/0db36216de7a42bf90de89b901ca6102`.

Crompton, O., G. G. Katul, and S. Thompson
2020. Resistance formulations in shallow overland flow along a hillslope covered with patchy vegetation. *Water Resources Research*, P. e2020WR027194.

Crompton, O., A. Sytsma, and S. Thompson
2019. Emulation of the saint venant equations enables rapid and accurate predictions of infiltration and overland flow velocity on spatially heterogeneous surfaces. *Water Resources Research*.

Crompton, O. V.
2018. *Who's afraid of the Saint Venant Equations?(Everyone, so I replaced it with Machine Learning)*. PhD thesis, UC Berkeley.

Dagbovie, A. S. and J. A. Sherratt
2014. Pattern selection and hysteresis in the rietkerk model for banded vegetation in semi-arid environments. *Journal of The Royal Society Interface*, 11(99):20140465.

Deblauwe, V., N. Barbier, P. Couteron, O. Lejeune, and J. Bogaert
2008. The global biogeography of semi-arid periodic vegetation patterns. *Global Ecology and Biogeography*, 17(6):715–723.

D'Odorico, P., F. Laio, and L. Ridolfi
2006. Vegetation patterns induced by random climate fluctuations. *Geophysical Research Letters*, 33(19).

Dueben, P. D. and P. Bauer
2018. Challenges and design choices for global weather and climate models based on machine learning. *Geoscientific Model Development*, 11(10):3999–4009.

Dunkerley, D.
2018. Banded vegetation in some australian semi-arid landscapes: 20 years of field observations to support the development and evaluation of numerical models of vegetation pattern evolution. *Desert*, 23(2):165–187.

Dunkerley, D. L.
2002. Infiltration rates and soil moisture in a groved mulga community near alice springs, arid central australia: evidence for complex internal rainwater redistribution in a runoff–runon landscape. *Journal of Arid Environments*, 51(2):199–219.

Fiedler, F. and H. A. Panofsky
1970. Atmospheric scales and spectral gaps. *Bulletin of the American Meteorological Society*, 51(12):1114–1120.

Gandhi, P., S. Bonetti, S. Iams, A. Porporato, and M. Silber
2019. A fast-slow model of banded vegetation pattern formation in drylands. *arXiv preprint arXiv:1911.08454*.

Giorgi, F., E.-S. Im, E. Coppola, N. Diffenbaugh, X. Gao, L. Mariotti, and Y. Shi
2011. Higher hydroclimatic intensity with global warming. *Journal of Climate*, 24(20):5309–5324.

Guttal, V. and C. Jayaprakash
2007. Self-organization and productivity in semi-arid ecosystems: Implications of seasonality in rainfall. *Journal of theoretical biology*, 248(3):490–500.

HilleRisLambers, R., M. Rietkerk, F. van den Bosch, H. H. Prins, and H. de Kroon
2001. Vegetation pattern formation in semi-arid grazing systems. *Ecology*, 82(1):50–61.

Istanbulluoglu, E. and R. L. Bras
2005. Vegetation-modulated landscape evolution: Effects of vegetation on landscape processes, drainage density, and topography. *Journal of Geophysical Research: Earth Surface*, 110(F2).

Katul, G., C.-T. Lai, K. Schäfer, B. Vidakovic, J. Albertson, D. Ellsworth, and R. Oren
2001. Multiscale analysis of vegetation surface fluxes: from seconds to years. *Advances in Water Resources*, 24(9-10):1119–1132.

Kéfi, S., M. Rietkerk, C. L. Alados, Y. Pueyo, V. P. Papanastasis, A. ElAich, and P. C. De Ruiter
2007. Spatial vegetation patterns and imminent desertification in mediterranean arid ecosystems. *Nature*, 449(7159):213.

Kefi, S., M. Rietkerk, and G. G. Katul
2008. Vegetation pattern shift as a result of rising atmospheric co2 in arid ecosystems. *Theoretical population biology*, 74(4):332–344.

Kharin, V. V., F. Zwiers, X. Zhang, and M. Wehner
2013. Changes in temperature and precipitation extremes in the cmip5 ensemble. *Climatic change*, 119(2):345–357.

Klausmeier, C. A.
1999. Regular and irregular patterns in semiarid vegetation. *Science*, 284(5421):1826–1828.

Kletter, A., J. Von Hardenberg, E. Meron, and A. Provenzale
2009. Patterned vegetation and rainfall intermittency. *Journal of theoretical biology*, 256(4):574–583.

Krasnopolsky, V. M. and M. S. Fox-Rabinovitz
2006. Complex hybrid models combining deterministic and machine learning components for numerical climate modeling and weather prediction. *Neural Networks*, 19(2):122–134.

Kumar, B., G. Sreenivasulu, and A. Ramakrishna Rao
2010. Metamodel-based design of alluvial channels at incipient motion subjected to seepage. *Hydrological Sciences Journal–Journal des Sciences Hydrologiques*, 55(3):459–466.

Mander, L., S. C. Dekker, M. Li, W. Mio, S. W. Punyasena, and T. M. Lenton
2017. A morphometric analysis of vegetation patterns in dryland ecosystems. *Royal Society open science*, 4(2):160443.

McGrath, G., K. Paik, and C. Hinz
2011. Complex landscapes from simple ecohydrological feedbacks. In *MODSIM2011, 19th International Congress on Modelling and Simulation*, Pp. 2528–2534. Model. and Simul. Soc. of Australia and New Zealand Canberra.

Meron, E.
2015. *Nonlinear physics of ecosystems*. CRC Press.

Meron, E.
2016. Pattern formation–a missing link in the study of ecosystem response to environmental changes. *Mathematical biosciences*, 271:1–18.

Michaelis, L. and M. L. Menten
1913. The kinetics of the inversion effect. *Biochem. Z*, 49:333–369.

Murray, J. D.
2003. *Mathematical Biology: I. An Introduction*.

Neelakantan, T. and N. Pundarikanthan
2000. Neural network-based simulation-optimization model for reservoir operation. *Journal of water resources planning and management*, 126(2):57–64.

Paschalis, A., G. G. Katul, S. Fatichi, G. Manoli, and P. Molnar
2016. Matching ecohydrological processes and scales of banded vegetation patterns in semiarid catchments. *Water Resources Research*, 52(3):2259–2278.

Penny, G. G., K. E. Daniels, and S. E. Thompson
2013. Local properties of patterned vegetation: quantifying endogenous and exogenous effects. *Phil. Trans. R. Soc. A*, 371(2004):20120359.

Prein, A. F., R. M. Rasmussen, K. Ikeda, C. Liu, M. P. Clark, and G. J. Holland
2017. The future intensification of hourly precipitation extremes. *Nature Climate Change*, 7(1):48.

Pueyo, Y., S. Kéfi, C. Alados, and M. Rietkerk
2008. Dispersal strategies and spatial organization of vegetation in arid ecosystems. *Oikos*, 117(10):1522–1532.

Raper, S. and U. Cubasch
1996. Emulation of the results from a coupled general circulation model using a simple climate model. *Geophysical Research Letters*, 23(10):1107–1110.

Razavi, S., B. A. Tolson, and D. H. Burn
2012. Numerical assessment of metamodelling strategies in computationally intensive optimization. *Environmental Modelling & Software*, 34:67–86.

Rietkerk, M., M. C. Boerlijst, F. van Langevelde, R. HilleRisLambers, J. v. de Koppel, L. Kumar, H. H. Prins, and A. M. de Roos
2002. Self-organization of vegetation in arid ecosystems. *The American Naturalist*, 160(4):524–530.

Rietkerk, M., S. C. Dekker, P. C. De Ruiter, and J. van de Koppel
2004. Self-organized patchiness and catastrophic shifts in ecosystems. *Science*, 305(5692):1926–1929.

Rietkerk, M. and J. Van de Koppel
2008. Regular pattern formation in real ecosystems. *Trends in ecology & evolution*, 23(3):169–175.

Rogers, L. L. and F. U. Dowla
1994. Optimization of groundwater remediation using artificial neural networks with parallel solute transport modeling. *Water Resources Research*, 30(2):457–481.

Rohmer, J., D. Idier, F. Paris, R. Pedreros, and J. Louisor
2018. Casting light on forcing and breaching scenarios that lead to marine inundation: Combining numerical simulations with a random-forest classification approach. *Environmental Modelling & Software*, 104:64–80.

Römkens, M. J., K. Helming, and S. Prasad
2002. Soil erosion under different rainfall intensities, surface roughness, and soil water regimes. *Catena*, 46(2-3):103–123.

Rossi, M., J. Ares, E. Jobbágy, E. Vivoni, R. Vervoort, A. Schreiner-McGraw, and P. Saco
2018. Vegetation and terrain drivers of infiltration depth along a semiarid hillslope. *Science of the Total Environment*, 644:1399–1408.

Saco, P., G. Willgoose, and G. Hancock
2007. Eco-geomorphology of banded vegetation patterns in arid and semi-arid regions.

Schlesinger, W. H. and A. M. Pilmanis
1998. Plant-soil interactions in deserts. *Biogeochemistry*, 42(1-2):169–187.

Seghieri, J., S. Galle, J.-L. Rajot, and M. Ehrmann
1997. Relationships between soil moisture and growth of herbaceous plants in a natural vegetation mosaic in niger. *Journal of Arid Environments*, 36(1):87–102.

Siteur, K., M. B. Eppinga, D. Karssenberg, M. Baudena, M. F. Bierkens, and M. Rietkerk
2014. How will increases in rainfall intensity affect semiarid ecosystems? *Water Resources Research*, 50(7):5980–6001.

Smith, M. W., N. J. Cox, and L. J. Bracken
2007. Applying flow resistance equations to overland flows. *Progress in Physical Geography*, 31(4):363–387.

Sreekanth, J. and B. Datta
2010. Multi-objective management of saltwater intrusion in coastal aquifers using genetic programming and modular neural network based surrogate models. *Journal of Hydrology*, 393(3-4):245–256.

Thompson, S., C. Harman, P. Heine, and G. Katul
2010. Vegetation-infiltration relationships across climatic and soil type gradients. *Journal of Geophysical Research: Biogeosciences*, 115(G2).

Thompson, S. and G. Katul
2009. Secondary seed dispersal and its role in landscape organization. *Geophysical Research Letters*, 36(2).

Thompson, S. and G. Katul
2011. Inferring ecosystem parameters from observation of vegetation patterns. *Geophysical Research Letters*, 38(20).

Thompson, S., G. Katul, A. Konings, and L. Ridolfi
2011a. Unsteady overland flow on flat surfaces induced by spatial permeability contrasts. *Advances in water resources*, 34(8):1049–1058.

Thompson, S. E., C. J. Harman, P. A. Troch, P. D. Brooks, and M. Sivapalan
2011b. Spatial scale dependence of ecohydrologically mediated water balance partitioning: A synthesis framework for catchment ecohydrology. *Water Resources Research*, 47(10).

Tongway, D. J. and J. A. Ludwig
1990. Vegetation and soil patterning in semi-arid mulga lands of eastern australia. *Australian Journal of Ecology*, 15(1):23–34.

Tongway, D. J. and J. A. Ludwig
2001. Theories on the origins, maintenance, dynamics, and functioning of banded landscapes. In *Banded vegetation patterning in arid and semiarid environments*, Pp. 20–31. Springer.

Ursino, N. and S. Contarini
2006. Stability of banded vegetation patterns under seasonal rainfall and limited soil moisture storage capacity. *Advances in Water Resources*, 29(10):1556–1564.

van de Koppel, J., M. Rietkerk, F. van Langevelde, L. Kumar, C. A. Klausmeier, J. M. Fryxell, J. W. Hearne, J. van Andel, N. de Ridder, A. Skidmore, et al.
2002. Spatial heterogeneity and irreversible vegetation change in semiarid grazing systems. *The American Naturalist*, 159(2):209–218.

Vincenot, C. E., F. Carteni, S. Mazzoleni, M. Rietkerk, and F. Giannino
2016. Spatial self-organization of vegetation subject to climatic stress—insights from a system dynamics—individual-based hybrid model. *Frontiers in plant science*, 7:636.

Watson, D. and J. Laflen
1986. Soil strength, slope, and rainfall intensity effects on interrill erosion. *Transactions of the ASAE*, 29(1):98–0102.

Welter, D. E., J. T. White, R. J. Hunt, and J. E. Doherty
2015. Approaches in highly parameterized inversion—pest++ version 3, a parameter estimation and uncertainty analysis software suite optimized for large environmental models. Technical report, US Geological Survey.

Westra, S., H. Fowler, J. Evans, L. Alexander, P. Berg, F. Johnson, E. Kendon, G. Lenderink, and N. Roberts
2014. Future changes to the intensity and frequency of short-duration extreme rainfall. *Reviews of Geophysics*, 52(3):522–555.

Yan, S. and B. Minsker
2003. A dynamic meta-model approach to genetic algorithm solution of a risk-based groundwater remediation design model. In *World Water & Environmental Resources Congress 2003*, Pp. 1–10.